INTERNATIONAL JOURNAL OF HYDROGEN ENERGY 39 (2014) 19767–19779

Available online at www.sciencedirect.com

ScienceDirect

journal homepage: www.elsevier.com/locate/he

Numerical analysis of anion-exchange membrane direct glycerol fuel cells under steady state and dynamic operations

Xiaotong Han [1,2], David J. Chadderdon [1,2], Ji Qi [1], Le Xin, Wenzhen Li[*,1], Wen Zhou[**]

Department of Chemical Engineering, Michigan Technological University, 1400 Townsend Drive, Houghton, MI 49931, USA

ARTICLE INFO

Article history:
Received 3 June 2014
Received in revised form
26 August 2014
Accepted 28 August 2014
Available online 13 October 2014

Keywords:
Fuel cell
Dynamic simulation
Glycerol oxidation
Gold nanoparticles
Mass transport

ABSTRACT

This work develops a one-dimensional model of an alkaline anion-exchange membrane direct glycerol fuel cell (AEM-DGFC) for cogeneration of tartronate and electricity. The model is validated against steady state and dynamic experiments, and shows good agreement. Steady state modeling includes anode and cathode losses and predicts the single cell polarization and power density curves. Coupled mass transport, charge transport, and electrochemical kinetics predict the effects of varying reactant concentration and diffusion layer porosity on single cell performance. The results show that anode overpotential is the major source of loss at middle to high current density regions, due to limited glycerol diffusion at the catalyst layer. Furthermore, the dynamic response of AEM-DGFC to step changes in current density is simulated by considering time-dependent species transport and double-layer capacitance charging. Analysis of dynamic simulation reveals that the liquid-phase reactant diffusion is a key factor influencing the transient AEM-DGFC behavior and is very sensitive to diffusion layer design. This new numerical analysis of a glycerol-fed fuel cell demonstrates that a simple, single oxidation product model can successfully predict the steady state and dynamic losses.

Copyright © 2014, Hydrogen Energy Publications, LLC. Published by Elsevier Ltd. All rights reserved.

Introduction

The increasingly urgent need for renewable sources of energy and fine chemicals to replace petroleum has driven huge efforts to develop sustainable and economically-feasible catalytic processes for the refinement of natural materials [1–4]. Being a polyol which is massively produced during biodiesel manufacturing, glycerol is considered a key biorenewable building-block for the production of many chemicals [5]. Among them, fine chemicals including glyceric acid (GA), tartronic acid (TA) and mesoxalic acid (MA) are products of glycerol oxidation reaction (GOR) [6]. Aqueous phase selective

* *Corresponding author*. Tel.: +1 515 294 4582; fax: +1 515 294 2689.
** *Corresponding author*. Tel.: +1 906 487 1164.
E-mail addresses: wzli@iastate.edu, liwenzhen@gmail.com (W. Li), wzhou1@mtu.edu (W. Zhou).
[1] Current address: Department of Chemical and Biological Engineering, Iowa State University, Ames, IA 50011, USA.
[2] Xiaotong Han and David J. Chadderdon contributed equally to this work.
http://dx.doi.org/10.1016/j.ijhydene.2014.08.144
0360-3199/Copyright © 2014, Hydrogen Energy Publications, LLC. Published by Elsevier Ltd. All rights reserved.

oxidation of glycerol to valuable chemicals over metal catalysts with O_2, air, or H_2O_2 oxidants is a very attractive green process due to its low environmental impact, and has been exhaustively researched [5–20]. However, conventional heterogeneous catalytic oxidation of glycerol cannot take advantage of the energy stored in the chemical bonds of glycerol, which can be converted directly into electrical energy through electrochemical oxidation in a fuel cell type reactor.

Low-temperature anion-exchange membrane fuel cells (AEMFC) have attracted enormous attention, owing to fast electrochemical kinetics, reduced fuel crossover, and a friendly alkaline environment allowing use of non-platinum catalyst [21]. Anion-exchange membrane direct glycerol fuel cells (AEM-DGFCs) are of special interest for the prospect of simultaneously producing electricity and valuable oxidation products [22–28]. Significant works on AEM-DGFC have made progress in improving electrical energy generation performance, however output power density remains limited by low selectivity to completely oxidized CO_2 or other deeply oxidized carboxylates [28]. Recently, Zhang et al. discovered that deep oxidation of glycerol (to TA and MA) was greatly facilitated with carbon-cloth based porous electrodes compared to smooth electrodes [29]. Even more recently, remarkable selectivity to TA (70.2% selectivity) was achieved on Au/C (carbon-supported gold nanoparticle catalyst) in an AEM-DGFC by tuning electrode structure and operating conditions [30]. Although much progress has been made in catalyst and reactor design through trail-and-error experiments for selective electrocatalytic oxidation, it remains a challenge to isolate the individual effects of mass transport, charge transport, and electrochemical kinetics on cell performance. However, mathematical modeling is a powerful and economical tool that, when combined with experimental results, may quantify those complicated physicochemical processes [31].

Previously, extensive fuel cell modeling works have focused on proton exchange membrane fuel cells (PEMFC) [32–36], however more recent efforts have been spent developing mathematical models of hydrogen, alcohol, and glucose-fed AEMFCs. An early one-dimensional, steady state study applied Tafel expressions to model electrode reactions and a multi-layer membrane model in order to study mass transport in an alkaline direct ethanol fuel cell [37]. Multi-dimensional, steady state and dynamic models were developed for the anode of H_2/O_2 AEMFC to study the effect of operating conditions on the transient distribution of liquid water in the anode [38,39]. An analytical model was recently reported for an alkaline membrane direct methanol fuel cell to identify the most significant factors affecting cell performance including methanol crossover and water transport limitations [40]. A three-dimensional, non-isothermal model of alkaline AEMFC was developed to study effects of anode humidification, water removal mechanisms, and water transport in the membrane [41]. Zhao's group recently published an elegant work on direct ethanol AEMFCs using a relatively simple one-dimensional model and assuming 100% selectivity to a single ethanol oxidation product, acetic acid [42]. This simplified approach was sufficient for investigating the effects of operating and design parameters on electricity generation performance. Similarly, a simple model of a direct glucose AEMFC considering mass transport and a single-product electrochemical oxidation reaction was developed, and found that unlike with other fuels, the anodic overpotential from glucose oxidation was quite large compared to the cathodic or ohmic losses [43]. However, to the best of our knowledge, such models have not been applied to glycerol fuel in AEMFC, partially as a result of the low selectivity to one particular GOR product previously achieved in anion-exchange membrane (AEM) reactors. Mathematical modeling of AEM-DGFC may reveal the unique behavior of glycerol as fuel, which has much higher viscosity and a greater number of electrons extracted from a single molecule (8.0 electrons for GLY to TA, compared to 4.0 electrons for ethanol oxidation to acetic acid) in oxidation compared to smaller alcohols such as ethanol and methanol.

Herein, a study of performance and behavior of AEM-DGFC with Au/C anode catalyst for cogeneration of electricity and TA, the most valuable GOR product, is conducted in terms of operating and structural design parameters. This work combines theoretical modeling, which integrates mass transport, charge transport, and electrochemical kinetics in steady state and dynamic domains with experimental testing for parameter determination and model validation. Steady state modeling predicts thermodynamic and kinetic losses under stable operating conditions, while the dynamic model reveals the dominant mechanisms of transient behavior under changing load conditions. Original laboratory experiments are performed to evaluate the steady state current–voltage relationship and dynamic responses to step changes in current density and AC current perturbations (EIS) in order to better understand and model the complex physicochemical processes of the AEM-DGFC.

Methods

Model formulation and assumptions

Fig. 1 shows the physical model domain including anode and cathode porous diffusion layers (DL) and catalyst layers (CL), separated by an anion-exchange membrane (AEM). GOR and oxygen reduction reaction (ORR) occur at the anode and cathode CLs, respectively, which are treated as interfaces with no physical thickness. Therefore, all mass transport resistance is represented in the porous DLs. The bulk flow channels

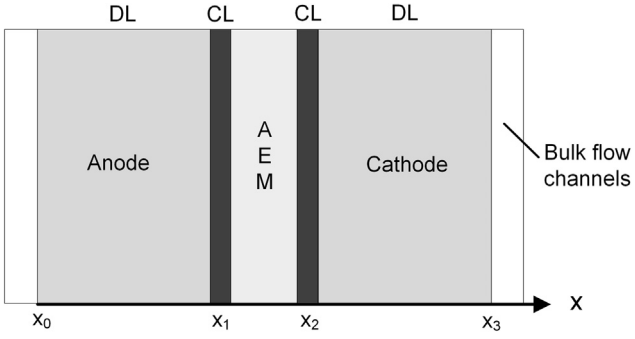

Fig. 1 – Schematic drawing of an AEM-DGFC and model domains including diffusion layers (DL), catalyst layers (CL), and anion-exchange membrane (AEM).

represent the boundary where fresh fuel is available at bulk concentrations, but are outside the model domain, which is bounded by points x_0 and x_3 in Fig. 1. Geometric dimensions and physical parameters of the model domain are shown in Table 1.

An important simplifying assumption is that GOR forms a single product, TA. We hypothesize that a single electrochemical oxidation reaction model can effectively predict the voltage losses and performance of an AEM-DGFC with Au/C anode catalyst due to the high product selectively (70.6% TA) recently achieved [30]. Theoretical standard cell potential is not overly sensitive to varying product distribution in this case, given that the standard cell potentials assuming GA, TA, or MA oxidation products are similar (*i.e.* 1.14, 1.17, or 1.12 V, respectively) [25]. Furthermore, the average number of electrons transferred experimentally on Au/C anode catalyst was estimated from reported product selectivity and ranged from 6.6 to 7.2 electrons per molecule GLY during a 12 h reaction (calculated from Ref. [30]), which is near the 8.0 electrons transferred for a single molecule of TA product used in this model. We propose that these values are sufficiently similar to predict the relationship between GLY molar consumption and faradaic current, which is critical for modeling species mass transport. The proposed model will be verified by comparison to original experimental tests under steady state and dynamic operations.

On the anode, GOR consumes GLY and hydroxideions (OH) and generates TA, water, and electrons:

$$C_3H_8O_3 + 8OH^- \rightarrow C_3H_4O_5 + 6H_2O + 8e^- \quad E_0^a = -0.77\ \text{V vs. SHE} \tag{1}$$

The generated TA is rapidly neutralized in alkaline solution and consumes 2 mol OH per mole TA to form tartronate ion (TAR):

$$C_3H_4O_5 + 2OH^- \rightarrow (C_3H_2O_5)^{2-} + 2H_2O \tag{2}$$

Product neutralization is a non-faradaic reaction and therefore does not contribute to the theoretical standard cell potential. On the cathode, oxygen reduction reaction (ORR) is the electron accepting reaction and also the generating source of OH:

$$2O_2 + 4H_2O + 8e^- \rightarrow 8OH^- \quad E_0^c = 0.40\ \text{V vs. SHE} \tag{3}$$

The generated OH at the cathode is transported through the AEM to the anode for GOR. The overall reaction including GOR, ORR, and TA neutralization becomes:

$$C_3H_8O_3 + 2O_2 + 2OH^- \rightarrow (C_3H_2O_5)^{2-} + 4H_2O \quad E_0 = 1.17\ \text{V} \tag{4}$$

In order to accurately model the desired electrochemical and physical phenomenon while maintaining reasonable calculation times, additional simplifications and approximations are made: (1) fuel cell operates under isothermal conditions, (2) reactant availability is predominately controlled by diffusion, while convective transport from bulk fluid flow and adsorption/desorption processes are neglected, (3) electrochemical reactions occur at the anode and cathode CLs, which are treated as interfaces with no thickness, and (4) species crossover through the membrane is ignored. Note that the Fe-based cathode catalyst is not active for GOR, so mixed-potentials from GLY crossover are not expected. Also, OH generated at the cathode is immediately available for GOR at the anode, however the resistance to ion transport is included in the calculation of cell voltage.

Table 1 – Geometric dimensions and physical parameters.

Parameter	Symbol	Value	Units	Reference
Porosity of anode DL	ε_{ADL}	0.56	–	Fitted
Porosity of cathode DL	ε_{CDL}	0.73	–	[42]
Thickness of anode DL	l_{ADL}	3.0×10^{-4}	m	Measured
Thickness of cathode DL	l_{CDL}	1.6×10^{-4}	m	Measured
Thickness of membrane	l_m	1.0×10^{-5}	m	[44]

Mass transport

Mass transport of reaction species is considered in the through-plane direction (*x*-direction, Fig. 1) and is assumed to be diffusion dominated and described by Fick's 2nd Law:

$$\frac{dC_i}{dt} = D_i^{eff}\frac{d^2C_i}{dx^2} \tag{5}$$

where C_i is concentration and D_i^{eff} is the effective diffusion coefficient of species *i*. For the steady state modeling, concentration does not change with time and the left-hand side of Fick's Law is zero. A numerical solution is found after applying physical and electrochemical boundary/initial conditions, described in later sections. The effective diffusion coefficient accounts for the porosity of anode or cathode DLs:

$$D_i^{eff} = \varepsilon^{3/2}D_i \tag{6}$$

where D_i is the species diffusion coefficient and ε is DL porosity. Porosity is difficult to measure because the DLs are under compression inside the fuel cell assembly and the transport properties can be significantly different than when uncompressed. Therefore, the anode DL porosity value is instead estimated based on the observed limiting current density in steady state experimental tests. Diffusion coefficients for GLY, OH, and TAR in water and O_2 in air are given at 333 K in Table 2. Little physical information is available on TAR, so the diffusion rates are approximated as equal to GLY, based on their similar molecular structure and size.

Table 2 – Mass and charge transport parameters.

Parameter	Symbol	Value	Units	Reference
Diffusion coefficient of GLY	D_{GLY}	2.824×10^{-9}	$m^2\ s^{-1}$	[45]
Diffusion coefficient of OH	D_{OH}	5.260×10^{-9}	$m^2\ s^{-1}$	[45]
Diffusion coefficient of TAR	D_{TAR}	2.824×10^{-9}	$m^2\ s^{-1}$	Assumed
Diffusion coefficient of O_2	D_{O_2}	2.742×10^{-5}	$m^2\ s^{-1}$	[45]
OH conductivity of membrane	σ_m	3.8	$(\Omega\ m)^{-1}$	[44]
Contact resistance	$R_{contact}$	4.48×10^{-6}	$\Omega\ m^2$	Measured[a]

[a] Total ohmic resistance measured by current-interrupt method minus membrane resistance.

Electrochemical kinetics

The relationship of the faradaic current density (j) with electrode overpotential (η) is given by the Butler–Volmer equation [46] and shown for GOR at the anode (a) and ORR at the cathode (c):

$$j_a = -j_{0,a}\left[\exp\left(\frac{\alpha_a F}{RT}\eta_a\right) - \exp\left(\frac{-(1-\alpha_a)F}{RT}\eta_a\right)\right] \quad (7)$$

$$j_c = j_{0,c}\left[\exp\left(\frac{-\alpha_c F}{RT}\eta_c\right) - \exp\left(\frac{(1-\alpha_c)F}{RT}\eta_c\right)\right] \quad (8)$$

where j_0 is exchange current density, α is transfer coefficient, and η is overpotential defined as:

$$\eta = E - E^0 \quad (9)$$

Electrode overpotential is defined here as the variation of potential from the standard potential, rather than reversible potential predicted by the Nernst equation, since the effect of changing bulk concentrations was quite small compared to the magnitude of standard potentials. Physicochemical parameters and constants are shown in Table 3. Overpotential is a combination of purely kinetic activation and additional concentration overpotentials that occur when reactant concentrations at CLs fall below reference values due to mass transport limitations. The concentration dependency of exchange current density is adapted from Ref. [35]:

$$j_{0,a} = j_{0,a}^{ref}\left(\frac{C_{GLY}^{CL}}{C_{GLY}^{ref}}\right)^{\gamma_{GLY}}\left(\frac{C_{OH}^{CL}}{C_{OH}^{ref}}\right)^{\gamma_{OH}} \quad (10)$$

$$j_{0,c} = j_{0,c}^{ref}\left(\frac{C_{O_2}^{CL}}{C_{O_2}^{ref}}\right)^{\gamma_{O_2}} \quad (11)$$

where (C_i^{CL}/C_i^{ref}) is the ratio of species concentration at the catalyst layer to the reference value, and γ is reaction order, assumed to be 1.0.

Table 3 – Physicochemical parameters and constants.

Parameter	Symbol	Value	Units	Reference
Anode standard potential	E_a^0	−0.77	V *vs.* SHE	[25]
Cathode standard potential	E_c^0	0.40	V *vs.* SHE	[25]
Number of electrons transferred	n	8.0	–	[25]
Anode exchange current density	$j_{0,a}$	4.0	A m^{-2}	Fitted
Cathode exchange current density	$j_{0,c}$	0.31	A m^{-2}	Fitted
Anode transfer coefficient	α_a	0.42	–	Fitted
Cathode transfer coefficient	α_c	0.58	–	Fitted
DLC of anode CL	$C_{eff,a}$	653	F m^{-2}	EIS
DLC of cathode CL	$C_{eff,c}$	653	F m^{-2}	EIS
Universal gas constant	R	8.314	J (mol K)$^{-1}$	–
Faraday's constant	F	96,485.3	C mol^{-1}	–

Double-layer capacitance

Energy is stored in or released from the reaction interface when electrode potential changes, due to charging or discharging of the electric double layer capacitance (DLC). The current associated with the charging/discharging contributes to cell current density (I_{cell}), but not the faradaic currents densities (j_a, j_c). As a result, DLC effectively smoothens the faradaic current response to a change in conditions, and the time response is dependent on the effective capacitance (C_{eff}) of the electrode DLC:

$$C_{eff}^a\frac{d\eta_a}{dt} = I_{cell} - |j_a| \quad (12)$$

$$C_{eff}^c\frac{d\eta_a}{dt} = I_{cell} - |j_c| \quad (13)$$

where the left-hand side represents the DLC charging/discharging current. At steady state the DLC behaves like an open-circuit and relationship of cell and faradaic currents simplifies to:

$$I_{cell} = |j_a| = |j_c| \quad (14)$$

Cell voltage

Cell voltage is calculated as:

$$V_{cell} = E_{cell}^0 - |\eta_a| - |\eta_c| - I_{cell}\left(R_{contact} + \frac{l_m}{\sigma_m}\right) \quad (15)$$

where E_{cell}^0 is the standard cell potential $(E_c^0 - E_a^0)$, $R_{contact}$ is the bulk contact resistance, and l_m/σ_m is the membrane resistance.

Numerical solution to AEM-DGFC models

The coupled system of mass transport, electrochemical kinetics, and cell voltage equations was solved using finite element methods in a commercial software package, COMSOL Multiphysics®. The boundary and initial conditions from Table 4 were applied. A linear interval was constructed to interpret the 1-D geometry domain, and was divided into 100 elements by applying a mesh grid. Each element was 0.003 mm, which resulted in good solution resolution. Steady state polarization tests were simulated using a parametric sweep of voltage or current. Dynamic operation tests were simulated using a second-order backward differentiation formula to discretize time derivatives and a PARDISO direct linear solver to predict the response to step changes in cell current density.

Experimental methods

Original laboratory experiments were performed on an AEM-DGFC with Au/C anode catalyst to verify the mathematical model and extract key modeling parameters. Detailed experimental setup of the fuel cell and testing station and catalyst synthesis details were given in previous publications and only new methods are covered here [27,30].

AEM-DGFC setup and testing methods

Fuel cell tests were performed on 850e Scribner fuel cell test stand with a 5.0 cm^2 fuel cell fixture (Fuel Cell Technologies). The anode catalyst was self-prepared Au/C (55 wt% Au)

Table 4 – Initial and boundary conditions.

Condition	Domain	Parameter	Value	Units
Dirichlet boundary:	$x = x_0$	C_i	C_i^{ref}	M
	$x = x_3$	C_{O_2}	$C_{O_2}^{ref}$	M
Neumann boundary:	$x = x_1$	N_i	$\lvert j_a \rvert s_i / nF$	mol m^{-2} s^{-1}
	$x = x_2$	N_{O_2}	$\lvert j_c \rvert s_{O_2} / nF$	mol m^{-2} s^{-1}
Initial conditions:	$x = x_0 \rightarrow x_1$	C_i	C_i^{bulk}	M
($t = 0$)		C_{O_2}	0	M
	$x = x_2 \rightarrow x_3$	C_i	0	M
		C_{O_2}	$C_{O_2}^{bulk}$	M

i = GLY, TAR, or OH.

prepared by aqueous-phase reduction method, blended with PTFE (5.0 wt% PTFE) and applied to a carbon-cloth liquid diffusion layer. The cathode used non-noble metal catalyst (Fe–Cu based 4020 catalyst, Acta), blended with AS-4 ionomer (Tokuyama), and applied directly to an AEM (A-901 Tokuyama, 10 μm). Carbon paper (Toray) was used as the cathode gas diffusion layer. Humidified high-purity O_2 (>99.999%) or air was fed into the cathode compartment at atmospheric back-pressure and 0.4 L min^{-1}. The cathode fuel and cell temperature were kept at 60 °C.

Steady state polarization curves were collected by sweeping current density from zero to the limiting condition by increments of 20 mA cm^{-2} and recording the cell voltage at each point. Each point was held for 2 min to ensure a stable cell voltage was recorded. The internal cell resistance (*IR*) was simultaneously measured using the current-interrupt technique. Additionally, a Hg/HgO (1.0 M KOH) reference electrode was inserted directly into the anode chamber and used to monitor the anode potential. Cathode potential (E_c) was calculated from the measured cell voltage, anode potential (E_a), and internal resistance by:

$$E_c = V_{cell} + E_a + IR \tag{16}$$

Experimental anode and cathode potentials were converted from V *vs.* Hg/HgO (1.0 M KOH) to SHE by adding 0.098 V [47]. Finally anode and cathode overpotentials at each current density were calculated from the standard electrode potentials with Equation (9).

The dynamic behavior of an AEM-DGFC was evaluated by performing step changes of current density and monitoring the cell voltage response over time. Current density step changes from 100 to 150 to 100 mA cm^{-2} were performed, with the cell voltage allowed to stabilize at each condition. The time to reach steady state was determined as the point where the studied variable changed less than 0.1% per second.

Electrochemical impedance spectroscopy (EIS) to estimate DLC

Electrochemical impedance spectroscopy (EIS), is a powerful diagnostic tool used to measure the frequency dependency of fuel cell impedance which uniquely capable to distinguish between the influences of different losses, such as membrane, charge transfer, mass transfer, and double-layer capacitance (DLC) [48]. Therefore, EIS was performed on an AEM-DGFC to estimate the effective capacitance of the DLC, which is a key parameter of the dynamic model. Two-electrode EIS tests were conducted at eight DC current set points ranging from 50 mA to 1.25 A. Frequency response analyzer (880 Impedance Analyzer, Scribner-Associates) applied AC perturbations with 5% of DC current amplitude to the load at frequencies sweeping from 10,000 to 0.1 Hz, and recorded the whole cell impedance response. EIS results were analyzed by fitting the equivalent circuit model shown in Fig. 2 to the measured impedance spectra with commercial electrochemistry software ZView (Scribner-Associates). Membrane and contact resistances depend on external cell current and were modeled as a single resistor (R_1) with a value set equal to total ohmic resistance previously measured by the current-interrupt method. Activation and concentration polarization are electrode phenomenon and depend on faradaic current, and therefore must be modeled in parallel with the DLC to account for the charging/discharging current at the electrode surface. Combined activation and concentration impedances were modeled as a resistor (R_2) in series with an inductor (L), to account for low-frequency inductive effects, and in parallel to the DLC. A constant phase element (CPE) was chosen to represent the DLC, in place of an ideal capacitor. CPE is a theoretical circuit element that is commonly used to model non-uniform capacitance along real electrode-membrane interfaces [49]. The effective capacitance of a CPE (C_{eff}) is estimated by:

$$C_{eff} = Q_o(\omega_{max})^{\varphi - 1} \tag{17}$$

where Q_o is the CPE time constant, ω_{max} is the angular frequency where maximum imaginary impedance occurs, and φ is the exponent of phase angle [50].

Results and discussion:

Steady state modeling of AEM-DGFC

Steady state operation and model validation

Experimental polarization and power density curves for AEM-DGFC under the operating conditions in Table 4 are shown in

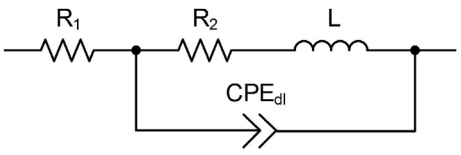

Fig. 2 – Equivalent circuit model diagram of AEM-DGFC impedances from ohmic losses (R_1), activation and concentration overpotentials (R_2), inductance (L), and double layer capacitance (CPE_{dl}).

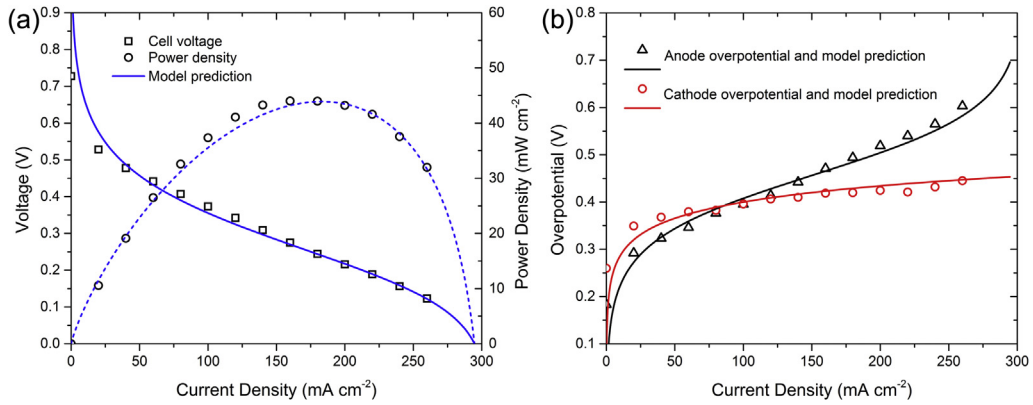

Fig. 3 – Experimental and predicted (a) polarization and power density curves and (b) absolute values of anode and cathode overpotentials *vs.* current density. Conditions: 60 °C; anode: 1.0 M GLY + 8.0 M OH; cathode: high purity O_2.

Fig. 3(a), together with the simulated results from steady state modeling for comparison. Important parameters of Butler–Volmer equation were determined by fitting the current–voltage behavior, including exchange current densities (j_0^{ref}) and transfer coefficients (α) for GOR and ORR (Table 3). However, fitting the model to cell voltage data alone cannot distinguish the individual contribution of losses from the anode and cathode reactions, so it was necessary to also consider the experimental anode and cathode overpotentials. Anode and cathode exchange current densities were found to be 4.0 A m^{-2} and 0.31 A m^{-2}, respectively and predicted overpotentials are shown *vs.* current density in Fig. 3(b), along with experimental results. Although Fig. 3(b) matches experimental data fairly well, the model does not predict the significant losses at OCV seen experimentally, which is a limitation of this kinetic model.

Specific voltage losses

Fig. 4 shows the specific overpotentials from ohmic, anode, and cathode losses *vs.* current density, simulated at conditions in Table 5. The ohmic losses, from bulk contact and membrane resistances, were found to be a minor contribution to total loss in the AEM-DGFC, which is partially explained by the high ionic conductivity and small thickness (10 μm) of the AEM. Anode losses were a combination of GOR kinetic activation and liquid-phase reactant (GLY, OH) concentration polarization. Cathode losses were almost entirely from ORR activation, while O_2 concentration polarization was negligible in the gas-phase cathode DL. It was found that cathode activation was the largest source of loss in the low current density range, due to relatively slow ORR kinetics under these conditions. Large ORR activation overpotentials are not surprising, when considering the use of the non-noble metal cathode catalyst and ambient pressure O_2 supply. Yet, anode overpotential became dominant in the middle current region, as mass transport limitations in the anode liquid DL were increased. The predicted results suggest that AEM-DGFC performance depends on a delicate balance of GOR and ORR activation losses with the anode concentration polarizations.

Effect of changing glycerol concentration

Fig. 5(a) shows predicted cell voltage and power density *vs.* current density for 0.50, 0.75, and 1.0 M bulk GLY concentrations. It is clear that cell performance was drastically decreased at lower bulk glycerol concentrations. Both peak power density and limiting current density were decreased corresponding to a sharp increase in anode overpotential at high current density, which is shown in Fig. 5(b), along with local GLY concentration at the anode catalyst layer (CL). It is well known that mass transport often dominates fuel cell performance in the high current density region. In the case of AEM-DGFC, liquid-phase diffusion of fuel through the porous anode DL was found to be a limiting factor due to the relatively slow diffusion rate of glycerol in aqueous solutions compared to other common fuels ($D_{Methanol,water}$ = 3.7 × 10^{-9} m^2 s^{-1}, $D_{GLY,water}$ = 2.8 × 10^{-9} m^2 s^{-1} at 333.15 K [45]). For instance, local glycerol concentration at the anode CL reached nearly zero at a current density of only 150 mA cm^{-2} when 0.5 M GLY was applied, and peak power density dropped by 40% to 26.2 mW cm^{-2}, compared to 43.9 mW cm^{-2} at 1.0 M GLY concentration. Relatively high concentrations of GLY alleviated the diffusion limitation due to the higher driving force for mass transport and improved cell performance, and

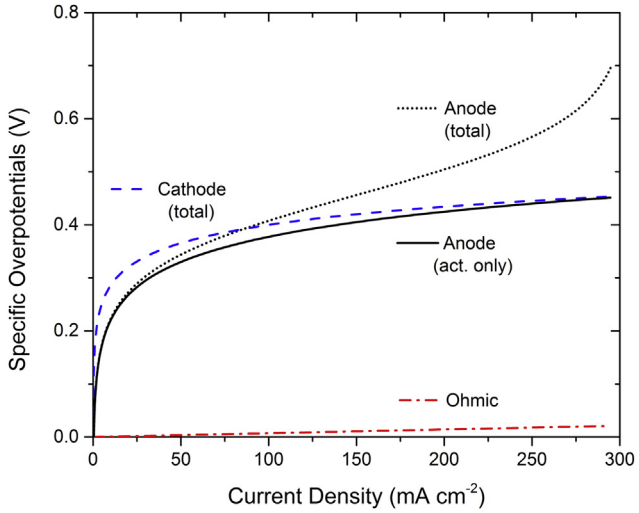

Fig. 4 – Specific absolute values of overpotentials from ohmic, anode (activation only and total), and cathode losses *vs.* current density.

Table 5 – Operation conditions and parameters.

Parameter	Symbol	Value	Units	Reference
Temperature	T	333.15	K	[30]
Cathode pressure	P	1.0	atm	[30]
Bulk concentration GLY	C_{GLY}^{bulk}	1.0	M	[30]
Bulk concentration OH	C_{OH}^{bulk}	8.0	M	[30]
Bulk concentration TAR	C_{TAR}^{bulk}	0	M	–
Bulk concentration O_2 (pure)	$C_{O_2}^{bulk}$	P/RT	M	–
Bulk concentration O_2 (air)	–	0.21 P/RT	M	–
Reference GLY concentration	C_{GLY}^{ref}	1.0	M	[30]
Reference OH concentration	C_{OH}^{ref}	8.0	M	[30]
Reference oxygen concentration	$C_{O_2}^{ref}$	P/RT	M	[30]

are therefore recommended for efficient and balanced AEM-DGFC operation.

Effect of changing alkaline *concentration*

Fig. 6(a) shows predicted cell voltage and power density *vs.* current density for 2.0, 4.0, and 6.0, and 8.0 M bulk OH concentrations. As with the GLY study, cell performance was decreased at lower OH concentration, however the effect was not as severe in this case. Cell voltage dropped slightly with decreasing bulk OH concentration from 8.0 to 4.0 M over the current density range, however the limiting current density was almost unchanged, only dropping from 295 to 283 mA cm^{-2}. However, when 2.0 M OH bulk was applied, local OH concentration was low enough (~1.0 M) to significantly limit the kinetics of GOR and resulted in additional concentration overpotential and both limiting current and peak power density were decreased. Fig. 6(b) reveals the relationship of anode overpotential and local OH concentration at the anode CL with changing bulk OH concentrations. It was found that the local OH concentration at the anode CL remained sufficiently high to facilitate GOR when at least 4.0 M OH was used, and it can be deduced that mass transport of GLY, not OH, was mainly limiting the cell performance. This demonstrates that although OH diffusivity is greater than glycerol (Table 2), mass transport limitations in the anode DL still may occur if proper operating conditions are not met. It should be noted that studies of other alkaline anion-exchange membrane fuel cell systems observed a "volcano-type" relationship of cell performance with base concentration, where increasing alkaline concentration was beneficial to a point, then had a negative effect above a tipping point concentration [51–53]. A proposed explanation comes from the competitive adsorption between OH and alcohol fuel, where too high base concentrations may prevent adequate alcohol adsorption to the active catalytic sites [54]. This phenomenon would not be predicted by this model since a main assumption is that reactant species availability is predominately diffusion controlled. However, in the future this can be considered by the addition of a surface reaction model that includes adsorption/desorption steps coupled with electrochemical surface reaction kinetics.

Effect of changing oxygen concentration

Cathode gas purity and pressure are critical parameters that determine the concentration of oxygen in the gas phase, and therefore also effect the ORR kinetics. However, using high purity and pressure O_2 may not always be practical solutions, due to added fuel costs. Fig. 7(a) and (b) show the steady state predictions of cell voltage and cathode overpotential, respectively, *vs.* current density using pure O_2 or air (21 mol% O_2) at ambient pressure. The cathode fed with air resulted in a decreased cell voltage of about 100 mV and a peak power density drop of about 30% compared to that with pure O_2. The cell voltage drop was caused by the decreased ORR kinetics and increased cathode overpotentials resulting from lowered O_2 bulk concentration. However, compared to GLY diffusivity in the liquid phase anode reaction/diffusion system, O_2 delivery in the gas phase is several magnitudes faster (Table 2) and additional mass transport limitations did not occur at high current densities. This was made evident by the limiting current density only decreasing from 295 to 278 mA cm^{-2} when fed with air and the flat cathode overpotential behavior at high current densities. In other terms, operation with pure O_2 achieves greater power density than air, but has little effect on the losses at high current density, which have been shown to be dominated by GLY diffusion in the anode DL.

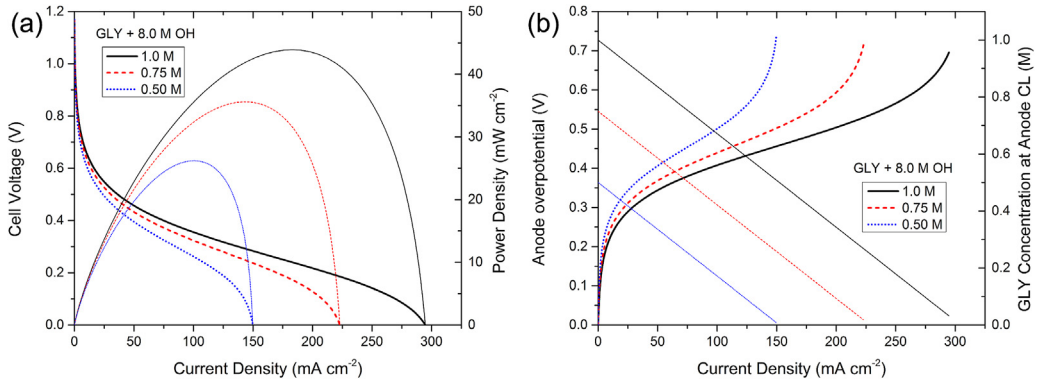

Fig. 5 – Predicted (a) polarization (bold) and power density curves (thin) and (b) anode overpotential (bold) and GLY concentration at anode CL (thin) for various GLY bulk concentrations.

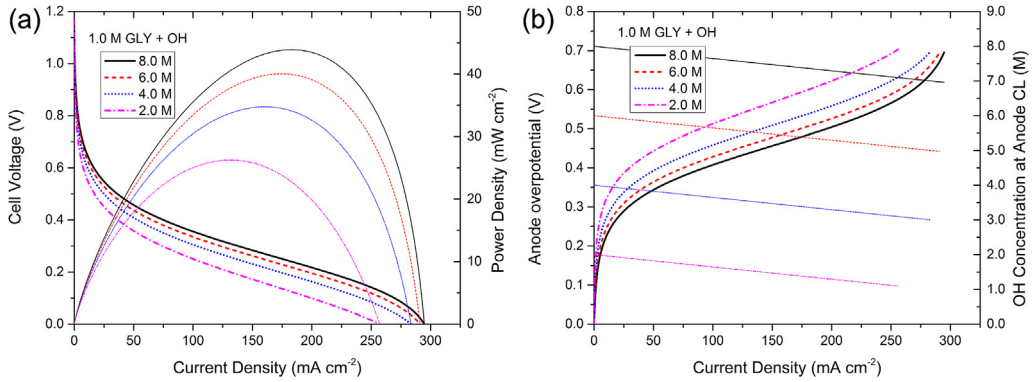

Fig. 6 – Predicted (a) polarization (bold) and power density curves (thin) and (b) anode overpotential (bold) and OH concentration at anode CL (thin) for various alkaline bulk concentrations.

Effect of changing anode DL porosity

Fig. 8(a) shows the predicted polarization and anode overpotentials *vs.* current density for anode DL porosity values ranging from 0.4 to 0.7. Cell performance was very sensitive to reactant species delivery at the anode, and even a small change in DL porosity resulted in significant difference in cell voltage when current density was greater than 100 mA cm^{-2}, the region where mass transport losses becomes evident. The decrease in cell voltage is attributed completely to the increased anode overpotentials as the DL porosity, and therefore effective diffusivities (Equation (5)) were decreased. Fig. 8(b) gives the GLY concentration profile within the anode DL at cell voltage of 0.1 V, where operation is close to the limiting current density. The GLY concentration gradient with respect to position became increasingly negative and the steady state concentration at the anode CL (position = 0.3 mm) varied from 188 to 50 mM as porosity decreased. The steady state parameter analysis of anode DL porosity demonstrated the high sensitivity of GOR to electrode design and mass transport resistances.

Dynamic modeling of AEM-DGFC

Dynamic operation and model verification

The time-dependent model was verified by comparison with experimental results of an AEM-DGFC operated with up/down step changes in current density. At the first step change, current density increased from 100 to 150 mA cm^{-2} and the model accurately predicted a rapid drop in cell voltage followed by gradual leveling, as shown in Fig. 9(a). Cell voltage stabilized to the value predicted by the steady state model, with little error compared to the experimental result. At the second step change, current density decreased from 150 to 100 mA cm^{-2} and cell voltage responded with a rapid increase before gradually returning to the steady state voltage. Due to the good agreement of the simulated and experimental results, we conclude that the model is a reasonable representation of the real dynamic mechanisms. Furthermore, the specific contributions of ohmic, activation, and concentration overpotentials to the dynamic cell voltage response were predicted and shown in Fig. 9(b). The change in ohmic loss includes ionic transport resistance in the AEM and bulk contact resistances, which are non-electrode processes and change instantaneously with current density in this model, as demonstrated by a vertical line at the time of step change. Kinetic activation is dependent on faradaic current, which does not vary instantaneously with cell current density due to DLC effects. However, it was found that activation overpotential reached the new steady state value very quickly, in less than 1 s. In contrast the concentration losses, which are also dependent on the DLC charging/discharging process, required much longer relaxation times to reach steady state

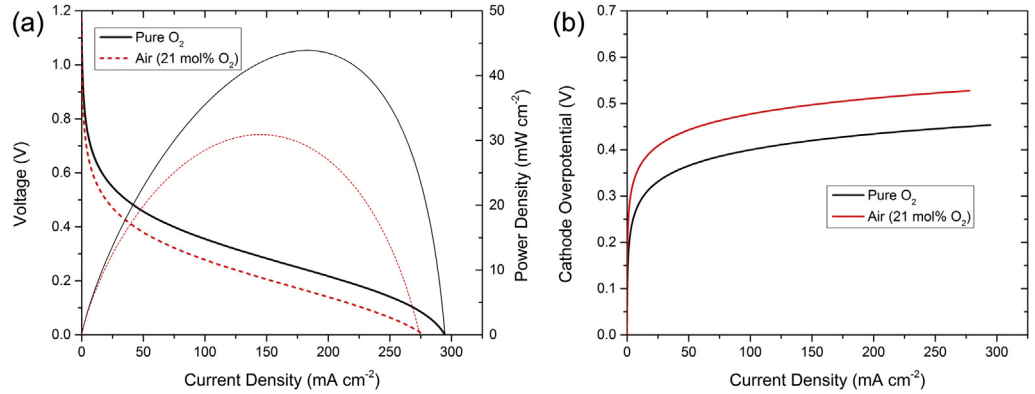

Fig. 7 – Predicted (a) polarization (bold) and power density (thin) curves and (b) absolute values of cathode overpotential for operation with high purity O_2 or air.

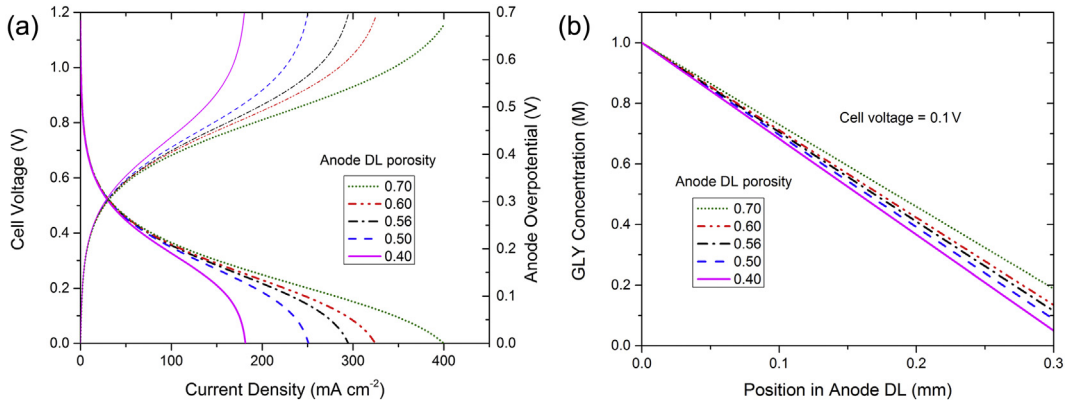

Fig. 8 – Predicted (a) polarization (bold) and anode overpotential (thin) curves and (b) GLY concentration profile through anode DL at cell voltage = 0.1 V for different anode DL porosities.

due to time-dependent species mass transport. Therefore, it can be concluded that the DLC effect is negligible in the AEM-DGFC when compared to the much slow diffusion processes which determine the dynamic behavior.

Identifying contributions of dynamic mechanisms with changing load conditions

Fuel cell dynamic response is controlled by complex physicochemical phenomena involving a wide range of time scales. Fig. 10(a) shows predicted overpotential split into the anodic and cathodic components for current density step changes of 100–150–100 mA cm^{-2}, in order to identify their contributions to the transient cell voltage response time. As seen in Fig. 10(a), and summarized in Table 6, cathode overpotential reached steady state about three magnitudes faster than anode overpotential. Even though anode and cathode overpotentials were both significant contributions to the steady state voltage loss under these conditions, the model predicts that the transient voltage behavior is mainly from the anode. This can be attributed to the far slower diffusion rates of GLY and OH in the liquid-phase anode DL compared to O_2 inside the gas-phase cathode DL. In order to more closely evaluate the transient anode losses, Fig. 10(b) shows predicted local anode species (GLY, OH) concentration and corresponding overpotentials over time in response to 100–150–100 mA cm^{-2} step changes. Fig. 10(b) shows that local GLY concentration at anode CL and GLY concentration overpotential reached steady state in a similar way over 132–140 s, while OH concentration reached steady state after only 73 s. The relatively slow anode dynamics are therefore attributed specifically to the non-steady state diffusion of GLY in the anode DL, based on the evidence that GLY stabilization occurred over the same approximate time scale as anode potential, and the fact that GLY concentration overpotential was about ten times greater contribution than that of OH.

Surprisingly, longer durations were needed for overpotentials and cell voltage to reach steady state for steps of increasing current density (step 1) than for decreasing current density (step 2). However, the time to reach steady state GLY concentration, which was the major contribution to transient behavior, did not depend on step direction. The explanation for this phenomenon comes from the governing equations of GLY mass transport and anode concentration overpotential. The first-order kinetics governing concentration loss gives

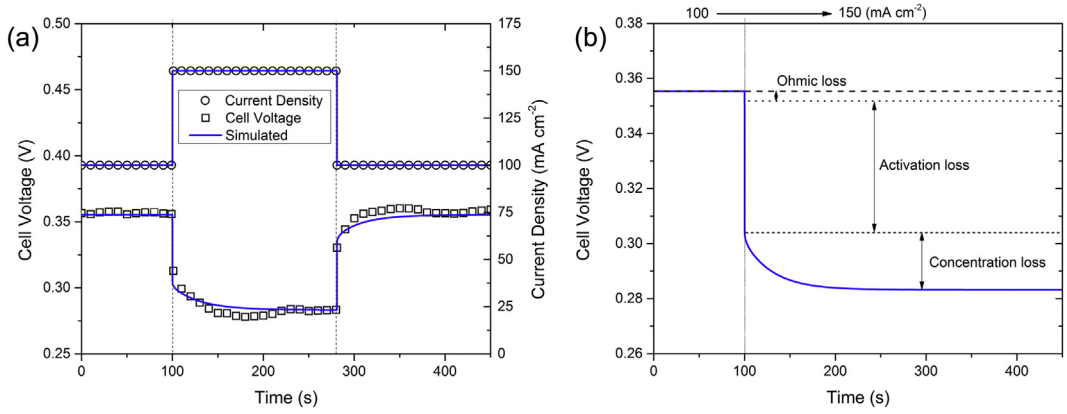

Fig. 9 – (a) Experimental and predicted dynamic response of cell voltage to up/down step changes in current density of 100–150–100 mA cm^{-2} and (b) specific contributions of ohmic, activation, and concentration overpotentials to dynamic response to 100–150 mA cm^{-2} step change.

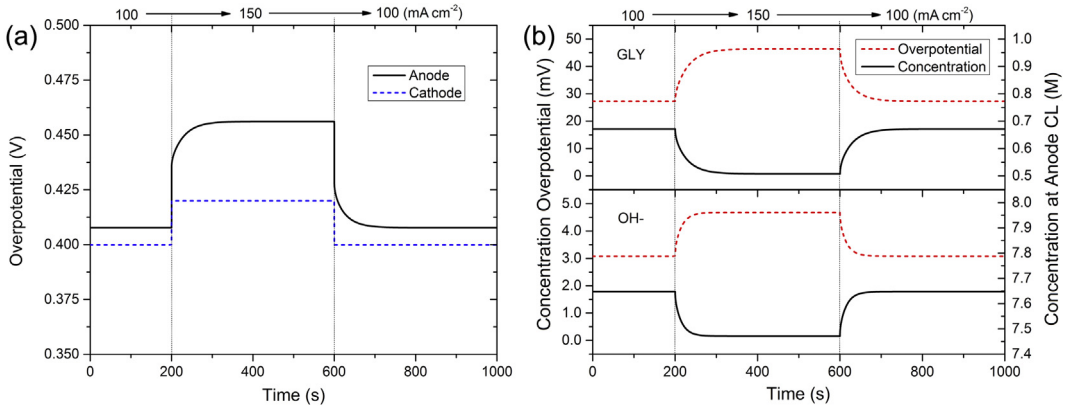

Fig. 10 – Predicted dynamic response of (a) absolute values of anode and cathode overpotentials and (b) GLY and OH concentrations at anode CL and concentration overpotentials to step changes of 100–150–100 mA cm^{-2}.

that overpotential is proportional to natural log of local GLY concentration, and therefore a derived relation for the rate of change of anode concentration overpotential is given by:

$$\frac{\partial \eta_{a,GLY}}{\partial t} \propto \left(\frac{1}{C_{GLY}} \frac{\partial C_{GLY}}{\partial t}\right) \quad (18)$$

where the rate of change of anode concentration overpotential from GLY is not only directly proportional to the rate of change of local GLY concentration but also inversely proportional to local GLY concentration. In effect, anode overpotential will reach a steady state value faster when GLY concentration is low, which corresponds to high current densities.

Effect of changing anode DL porosity on dynamic response

The dynamic cell behavior was strongly dependent on the transient mass transport of GLY and OH in the anode DL, and it may be desirable to alter the DL design to improve the response to changing conditions. Dynamic simulations were performed to explore the effects of anode DL porosity on the local GLY concentration response to 100–150–100 mA cm^{-2} step changes and results are summarized in Fig. 11 and Table 7. It is demonstrated that GLY concentration response time was very sensitive to anode DL porosity, reaching steady state faster with increasing porosity. While the anode DL must provide a solid, electrically conductive pathway for electron collection, it must also be sufficiently porous to allow efficient delivery and removal of reaction species. An anode DL with low porosity may be preferred to reduce electron transport resistance, however the effective diffusion rates of reaction species will suffer.

Table 6 – Dynamic responses of study parameters to 100–150–100 mA cm^{-2} step changes.

Study parameter	Step 1 (s)	Step 2 (s)
Cell voltage	100	91
Anode overpotential	112	104
Cathode overpotential	0.2	0.2
GLY concentration at CL	136	136
GLY concentration overpotential	140	132
OH concentration at CL	73	73
OH concentration overpotential	74	73

Estimating dynamic parameters with electrochemical impedance spectroscopy (EIS)

EIS spectra at DC current set points from 50 mA to 1.25 A are shown in Fig. 12. The observed Nyquist plots have the shape of a depressed semi-circle loop in the negative Z_{Im} region and a smaller loop in positive Z_{Im} that becomes more developed with higher current densities, associated with low-frequency inductive effects. The inductance loop observed in fuel cell EIS has been previously attributed to the relaxation of adsorbed intermediate species during multi-step electrode reactions [55]. Electrocatalytic oxidation of GLY on Au/C catalyst is a complex reaction involving adsorbed intermediates species [30], which could explain the observed inductance effect. However it is beyond the scope of this study to identify the specific contributions of the anode or cathode reactions.

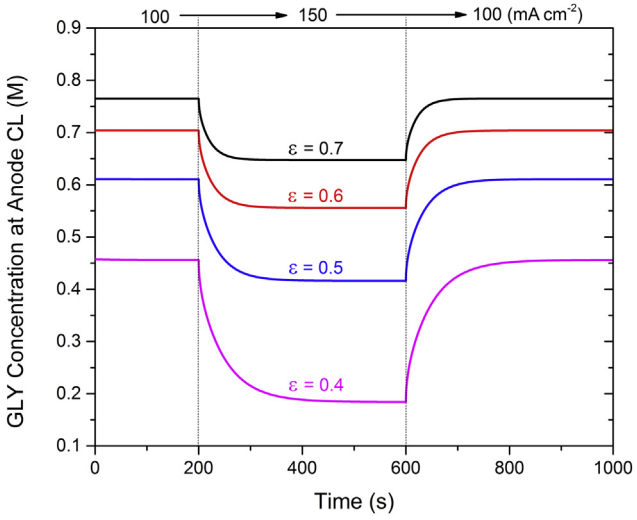

Fig. 11 – Predicted dynamic response of GLY concentration to step changes in current density of 100–150–100 mA cm^{-2} at different anode DL porosities.

Table 7 – Effect of changing anode DL porosity on dynamic response of GLY concentration to 100–150–100 mA cm^{-2} step changes.

Porosity	Steps 1 (s)	Step 2 (s)
$\varepsilon = 0.40$	225	225
$\varepsilon = 0.50$	161	161
$\varepsilon = 0.56$	136	136
$\varepsilon = 0.60$	123	123
$\varepsilon = 0.70$	98	98

The equivalent circuit model shown in Fig. 2 was fitted to the experimental impedance data by finding the optimized values of R_2, L, Q_o, and φ at each DC current, summarized in Supplementary Content, Table S1, along with a comparison of experimental cell resistance between EIS and steady state polarization tests. Note, a constant value of ohmic resistance (R_1) was assigned, as measured by the current-interrupt method. The 'goodness' of the equivalent circuit model fit was quantified by the weighted sum of squared error, which ranged from 0.346 to 2.87 $\times$ 10^{-2}. The greatest error was found for the lowest current, 0.05 A, at which point the observed inductance effect was diminished, which introduced error in the inductor circuit element.

In this method, EIS measures the combined impedances of anode and cathode, however the specific contributions of each electrode are not distinguishable from the single negative Z_{Im} loop observed. This is explained by one of two cases. First, the EIS spectra could be attributed to a single half-cell reaction if the other reaction occurs with negligible activation polarization, as is the case for H_2/O_2 PEM fuel cells where the hydrogen oxidation reaction at the anode is much more facile than ORR at the cathode [56–58]. Second, if the two half-cell time constants are comparable magnitudes then the two semi-circles merge and a single semi-circle is formed that corresponds to the total cell impedance [57]. We propose the second case for AEM-DGFC, since liquid-phase GOR occurs much slower than HOR, and was shown to have activation losses on the same magnitude as ORR (see Fig. 3(B)). Effective capacitance was calculated for each cell current from the fitted CPE parameters (Q_o and φ) and the frequency where maximum $-Z_{Im}$ occurred. The calculated values fluctuated near a mean value of 326 F m^{-2}, ranging from 261 to 366 F m^{-2}, based on geometric reactor area. Under the hypothesis that the anode and cathode impedances occur over the same time scale, it is reasonable to assume the half-cell effective capacitances are approximately equal. As a result, the half-cell capacitances are equal to two times the total capacitance, or 653 F m^{-2}, as calculated by the inverse rule of capacitances in series. To the best of our knowledge, no such parameter has been previously reported for an AEM-DGFC, however this value does fall within the range of 100–1000 F m^{-2}, previously reported in a classic DMFC impedance study [55].

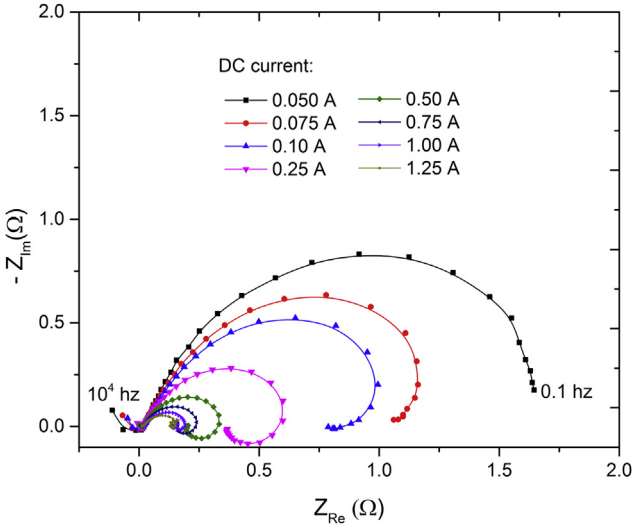

Fig. 12 – Nyquist plots of cell impedance from EIS tests at 0.05 A–1.25 A.

Recall that the dynamic response time of the DLC charging/discharging was found to be negligible compared to the slow diffusional processes. In fact, increasing the capacitance parameters by ten times resulted in the time to reach steady state cell voltage increasing by only ~1%, for a 100–150 mA cm^{-2} current density step. So, although the equivalent circuit method of estimating the effective capacitance relies some on averaging and estimation, the values are confidently within the correct magnitude of the true capacitance, and therefore are suitable for use in the dynamic AEM-DGFC model.

Conclusions

A simple, single-product kinetic model with one-dimensional species transport was developed which accurately predicted the steady state voltage losses and dynamic response to changing load conditions in an AEM-DGFC. Significant ORR activation overpotentials at the cathode contributed to losses in the low current density region, while anode overpotential was the major source of loss at middle to high current densities, due to limited glycerol diffusion in the catalyst layer. The effect of changing fuel concentration was investigated and it was found that performance was very sensitive to GLY bulk concentration, but high alkaline concentrations alleviated significant OH mass transport losses. Prediction of dynamic response of AEM-DGFC, including time-dependent species transport and DLC charging, to step changes in current density revealed that liquid-phase reactant diffusion was a key factor influencing the transient AEM-DGFC behavior and was very sensitive to diffusion layer design. In comparison, mass transport losses at the cathode were negligible due to fast O_2 transport in the gas-phase diffusion layer. As a result, the dynamic response of cathode overpotential was controlled by ORR activation losses and reached steady state quickly and therefore did not contribute to the overall cell response time. EIS with equivalent circuit modeling allowed parameter estimation of anode and cathode effective capacitances and further supported the dynamic model.

This work demonstrates a new mathematical model for AEM-DGFC, which accurately predicted cell performance and behavior under many simplifying assumptions. Future studies will build upon this work by incorporating: (1) multiple oxidation products and varying product selectivity, (2)

detailed reaction sequence of adsorption/desorption and surface reactions, (3) non-isothermal conditions with Arrhenius temperature-dependent rate law, and (4) species mass transport by convective flow. These additional complexities allow for more traditional kinetic analysis and form an even better representation of the physicochemical processes and selective oxidation in AEM-based alcohol fuel cells. The development of robust, validated theoretical simulations in parallel with advanced experimental techniques is critical for future breakthroughs in electrocatalytic production of chemicals and energy from biorenewables.

Acknowledgments

This work is partially supported by the U.S. National Science Foundation (CBET-1159448) and Michigan Tech REF-RS (E49290). J. Qi is grateful to financial support from the Chinese Scholarship Council.

Nomenclature

AEM	anion-exchange membrane
AEM-DGFC	anion-exchange membrane – direct glycerol fuel cell
CL	catalyst layer
CPE	constant phase element
D	diffusion coefficient
DL	diffusion layer
E	potential
F	Faraday's constant
GOR	glycerol oxidation reaction
I_{cell}	cell current density
j_0	exchange current density
ORR	oxygen reduction reaction
n	number of electrons transferred per molecule
N	molar flux
Q_o	first CPE coefficient
s	stoichiometric coefficient
V	voltage

Greek

α	transfer coefficient
ε	diffusion layer porosity
η	overpotential
σ	conductivity
ω	angular frequency
φ	second CPE coefficient

Sub/superscripts

a	anode
c	cathode
GLY	glycerol
i	chemical species
O_2	oxygen
OH	hydroxide ion
TA	tartronic acid
TAR	tartronate ion

Appendix A. Supplementary data

Supplementary data related to this article can be found at http://dx.doi.org/10.1016/j.ijhydene.2014.08.144.

REFERENCES

[1] Bozell JJ, Petersen GR. Technology development for the production of biobased products from biorefinery carbohydrates—the US Department of Energy's "Top 10" revisited. Green Chem 2010;12:539–54.
[2] Chheda JN, Huber GW, Dumesic JA. Liquid-phase catalytic processing of biomass-derived oxygenated hydrocarbons to fuels and chemicals. Angew Chem Int Ed 2007;46:7164–83.
[3] Corma A, Iborra S, Velty A. Chemical routes for the transformation of biomass into chemicals. Chem Rev 2007;107:2411–502.
[4] Gallezot P. Conversion of biomass to selected chemical products. Chem Soc Rev 2012;41:1538–58.
[5] Prati L, Spontoni P, Gaiassi A. From renewable to fine chemicals through selective oxidation: the case of glycerol. Top Catal 2009;52:288–96.
[6] Katryniok B, Kimura H, Skrzynska E, Girardon JS, Fongarland P, Capron M, et al. Selective catalytic oxidation of glycerol: perspectives for high value chemicals. Green Chem 2011;13:1960–79.
[7] Zope BN, Davis SE, Davis RJ. Influence of reaction conditions on diacid formation during Au-catalyzed oxidation of glycerol and hydroxymethylfurfural. Top Catal 2012;55:24–32.
[8] Zhou CH, Beltramini JN, Fana YX, Lu GQ. Chemoselective catalytic conversion of glycerol as a biorenewable source to valuable commodity chemicals. Chem Soc Rev 2008;37:527–49.
[9] Porta F, Prati L. Selective oxidation of glycerol to sodium glycerate with gold-on-carbon catalyst: an insight into reaction selectivity. J Catal 2004;224:397–403.
[10] Pagliaro M, Ciriminna R, Kimura H, Rossi M, Della Pina C. From glycerol to value-added products. Angew Chem Int Ed 2007;46:4434–40.
[11] Ketchie WC, Fang YL, Wong MS, Murayama M, Davis RJ. Influence of gold particle size on the aqueous-phase oxidation of carbon monoxide and glycerol. J Catal 2007;250:94–101.
[12] Ketchie WC, Murayama M, Davis RJ. Promotional effect of hydroxyl on the aqueous phase oxidation of carbon monoxide and glycerol over supported Au catalysts. Top Catal 2007;44:307–17.
[13] Dimitratos N, Villa A, Prati L. Liquid phase oxidation of glycerol using a single phase (Au–Pd) Alloy supported on activated carbon: effect of reaction conditions. Catal Lett 2009;133:334–40.
[14] Dimitratos N, Lopez-Sanchez JA, Hutchings GJ. Green catalysis with alternative feedstocks. Top Catal 2009;52:258–68.
[15] Carrettin S, McMorn P, Johnston P, Griffin K, Kiely CJ, Hutchings GJ. Oxidation of glycerol using supported Pt, Pd and Au catalysts. Phys Chem Chem Phys 2003;5:1329–36.
[16] Carrettin S, McMorn P, Johnston P, Griffin K, Kiely CJ, Attard GA, et al. Oxidation of glycerol using supported gold catalysts. Top Catal 2004;27:131–6.
[17] Carrettin S, McMorn P, Johnston P, Griffin K, Hutchings GJ. Selective oxidation of glycerol to glyceric acid using a gold catalyst in aqueous sodium hydroxide. Chem Commun 2002:696–7.

[18] Brett GL, He Q, Hammond C, Miedziak PJ, Dimitratos N, Sankar M, et al. Selective oxidation of glycerol by highly active bimetallic catalysts at ambient temperature under base-free conditions. Angew Chem Int Ed 2011;50:10136–9.
[19] Bianchi CL, Canton P, Dimitratos N, Porta F, Prati L. Selective oxidation of glycerol with oxygen using mono and bimetallic catalysts based on Au, Pd and Pt metals. Catal Today 2005;102–103:203–12.
[20] Villa A, Wang D, Veith GM, Prati L. Bismuth as a modifier of Au–Pd catalyst: enhancing selectivity in alcohol oxidation by suppressing parallel reaction. J Catal 2012;292:73–80.
[21] Bianchini C, Shen PK. Palladium-based electrocatalysts for alcohol oxidation in half cells and in direct alcohol fuel cells. Chem Rev 2009;109:4183–206.
[22] Bambagioni V, Bianchini C, Marchionni A, Filippi J, Vizza F, Teddy J, et al. Pd and Pt–Ru anode electrocatalysts supported on multi-walled carbon nanotubes and their use in passive and active direct alcohol fuel cells with an anion-exchange membrane (alcohol = methanol, ethanol, glycerol). J Power Sources 2009;190:241–51.
[23] Simões M, Baranton S, Coutanceau C. Electrochemical valorisation of glycerol. Chem Sus Chem 2012;5:2106–24.
[24] Zhang Z, Xin L, Li W. Supported gold nanoparticles as anode catalyst for anion-exchange membrane-direct glycerol fuel cell (AEM-DGFC). Int J Hydrogen Energy 2012;37:9393–401.
[25] Xin L, Zhang Z, Wang Z, Li W. Simultaneous generation of mesoxalic acid and electricity from glycerol on a gold anode catalyst in anion-exchange membrane fuel cells. ChemCatChem 2012:1105–14.
[26] Zhang Z, Xin L, Li W. Electrocatalytic oxidation of glycerol on Pt/C in anion-exchange membrane fuel cell: cogeneration of electricity and valuable chemicals. Appl Catal B. 2012;119-120:40–8.
[27] Zhang Z, Xin L, Qi J, Chadderdon DJ, Li W. Supported Pt, Pd and Au nanoparticle anode catalysts for anion-exchange membrane fuel cells with glycerol and crude glycerol fuels. Appl Catal B. 2013;136–137:29–39.
[28] Marchionni A, Bevilacqua M, Bianchini C, Chen YX, Filippi J, Fornasiero P, et al. Electrooxidation of ethylene glycol and glycerol on Pd–(Ni–Zn)/C anodes in direct alcohol fuel cells. Chem Sus Chem 2013;6:518–28.
[29] Zhang Z, Xin L, Qi J, Chadderdon DJ, Sun K, Warsko KM, et al. Selective electro-oxidation of glycerol to tartronate or mesoxalate on Au nanoparticle catalyst via electrode potential tuning in anion-exchange membrane electrocatalytic flow reactor. Appl Catal B. 2014;147:871–8.
[30] Qi J, Xin L, Chadderdon DJ, Qiu Y, Jiang Y, Benipal N, et al. Electrocatalytic selective oxidation of glycerol to tartronate on Au/C anode catalysts in anion exchange membrane fuel cells with electricity cogeneration. Appl Catal B 2014;154-155:360–8.
[31] Zawodzinski T, Wieckowski A, Mukerjee S, Neurock M. Integrated theoretical and experimental studies of fuel cell electrocatalysts. Electrochem Soc Interface 2007;16(2):37–41.
[32] Bernardi DM, Verbrugge MW. Mathematical model of a gas diffusion electrode bonded to a polymer electrolyte. AIChE J 1991;37:1151–63.
[33] Rowe A, Li X. Mathematical modeling of proton exchange membrane fuel cells. J Power Sources 2001;102:82–96.
[34] Berning T, Lu DM, Djilali N. Three-dimensional computational analysis of transport phenomena in a PEM fuel cell. J Power Sources 2002;106:284–94.
[35] Zhu H, Kee RJ. A general mathematical model for analyzing the performance of fuel-cell membrane-electrode assemblies. J Power Sources 2003;117:61–74.
[36] Wang CY. Fundamental models for fuel cell engineering. Chem Rev 2004;104:4727–66.
[37] Bahrami H, Faghri A. Multi-layer membrane model for mass transport in a direct ethanol fuel cell using an alkaline anion exchange membrane. J Power Sources 2012;218:286–96.
[38] Huo S, Deng H, Chang Y, Jiao K. Water management in alkaline anion exchange membrane fuel cell anode. Int J Hydrogen Energy 2012;37:18389–402.
[39] Deng H, Huo S, Chang Y, Zhou Y, Jiao K. Transient analysis of alkaline anion exchange membrane fuel cell anode. Int J Hydrogen Energy 2013;38:6509–25.
[40] Deng H, Chen J, Jiao K, Huang X. An analytical model for alkaline membrane direct methanol fuel cell. Int J Heat Mass Transf 2014;74:376–90.
[41] Jiao K, He P, Du Q, Yin Y. Three-dimensional multiphase modeling of alkaline anion exchange membrane fuel cell. Int J Hydrogen Energy 2014;39:5981–95.
[42] An L, Chai ZH, Zeng L, Tan P, Zhao TS. Mathematical modeling of alkaline direct ethanol fuel cells. Int J Hydrogen Energy 2013;38:14067–75.
[43] Pathak R, Basu S. Mathematical modeling and experimental verification of direct glucose anion exchange membrane fuel cell. Electrochim Acta 2013;113:42–53.
[44] Fuller T. Proton exchange membrane fuel cells 8. ECS Trans 2008;16:257–62.
[45] Yaws CL. Yaws' transport properties of chemicals and hydrocarbons (Electronic Edition). Elsevier, Inc.; 2010.
[46] Bard AJ, Faulkner LR. Electrochemical methods: fundamentals and applications. 2nd ed. John Wiley & Sons, Inc; 2001.
[47] Landolt D. Corrosion and surface chemistry of metals. EPFL Press; 2007.
[48] Chang BY, Park SM. Electrochemical impedance spectroscopy. Annu Rev Anal Chem 2010:207–29.
[49] Apartna DM, Dale NV, Salehfar H, Mann MD, Han T-H. Equivalent electric circuit modeling and performance analysis of a PEM fuel cell stack using impedance spectroscopy. IEEE Trans Energy Convers 2010;25:778–86.
[50] Hsu CH, Mansfeld F. Concerning the conversion of the constant phase element parameter Y0 into a capacitance. Corrosion 2001;57:747–8.
[51] Qi J, Xin L, Zhang Z, Sun K, He H, Wang F, et al. Surface dealloyed Pt nanoparticles supported on carbon nanotubes: facile synthesis and promising applications for direct crude glycerol anion-exchange membrane fuel cell. Green Chem 2013;15:1133–7.
[52] Li YS, Zhao TS, Liang ZX. Performance of alkaline electrolyte-membrane-based direct ethanol fuel cells. J Power Sources 2009;187:387–92.
[53] An L, Zhao TS, Shen SY, Wu QX, Chen R. Performance of a direct ethylene glycol fuel cell with an anion-exchange membrane. Int J Hydrogen Energy 2010;2010:4329–35.
[54] Spendelow JS, Wieckowski A. Electrocatalysis of oxygen reduction and small alcohol oxidation in alkaline media. Phys Chem Chem Phys 2007;9:2654–75.
[55] Muller JT, Urban PM, Holderich WF. Impedance studies on direct methanol fuel cell anodes. J Power Sources 1999;84:157–60.
[56] Springer E, Zawodzinski A, Wilson MS, Golfesfeld S. Characterization of polymer electrolyte fuel cells using AC impedance spectroscopy. J Electrochem Soc 1996;143:587–99.
[57] Gomadam PM, Weidner JW. Analysis of electrochemical impedance spectroscopy in proton exchange membrane fuel cells. Int J Energy Res 2005;29:1133–51.
[58] Yuan X, Wang H, Sun J, Zhang J. AC impedance technique in PEM fuel cell diagnosis – a review. Int J Hydrogen Energy 2007;32:4365–80.